

THE SHELLLESS SNR B0532–67.5 IN THE LARGE MAGELLANIC CLOUD

CHUAN-JUI LI (李傳睿)¹, YOU-HUA CHU (朱有花)¹, CHEN-YU CHUANG(莊鎮宇)¹,
GUAN-HONG LI (李冠宏)^{1,2}

¹ Institute of Astronomy and Astrophysics, Academia Sinica, No. 1, Sec. 4, Roosevelt Rd., Taipei 10617, Taiwan
cjli@asiaa.sinica.edu.tw, yhchu@asiaa.sinica.edu.tw

² Graduate Institute of Astrophysics, National Taiwan University, Taipei 10617, Taiwan.

Draft version November 15, 2021

ABSTRACT

The SNR B0532–67.5 in the Large Magellanic Cloud (LMC) was first diagnosed by its nonthermal radio emission and its SNR nature was confirmed by diffuse X-ray emission; however, no optical SNR shell is detected. The OB association LH75, or NGC 2011, is projected within the boundary of this SNR. We have analyzed the massive star population in and around SNR B0532–67.5: using optical photometric data to construct color-magnitude diagrams (CMDs), using stellar evolutionary tracks to estimate stellar masses, and using isochrones to assess the stellar ages. From these analyses, we find a 20–25 Myr population in LH75 and a younger population less than 10 Myr old to the southwest of LH75. The center of SNR B0532–67.5 is located closer to the core of LH75 than the massive stars to its southwest. We conclude that the SN progenitor was probably a member of LH75 with an initial mass $\sim 15 M_{\odot}$. The SN exploded in an H I cavity excavated by the energy feedback of LH75. The low density of the ambient medium prohibits the formation of a visible nebular shell. Despite the low density in the ambient medium, physical properties of the hot gas within the SNR interior do not differ from SNRs with a visible shell by more than a factor of 2–3. The large-scale H I map shows that SNR B0532–67.5 is projected in a cavity that appears to be connected with the much larger cavity of the supergiant shell LMC-4.

Subject headings: ISM: supernova remnants — ISM: individual objects (SNR B0532–67.5) — Magellanic Clouds

1. INTRODUCTION

Supernova remnants (SNRs) are commonly diagnosed by their diffuse X-ray emission, nebular shells with elevated [S II]/H α line ratios, and nonthermal radio spectral indices. These signatures are associated with SNR shocks going through the ambient medium, and their detection depends on the density of the medium and the sensitivity of observing facilities. For example, the XMM-Newton X-ray Observatory is able to detect the diffuse X-rays from an SNR whose ambient density is $> 10^{-3}$ H-atom cm^{-3} , while the commonly available CCD cameras with a narrow H α filter ($\Delta\lambda \sim 10 - 20 \text{ \AA}$) can detect an SNR shell only if the ambient density is greater than ~ 1 H-atom cm^{-3} (Ou et al. 2018). It is thus not surprising that some SNRs are diagnosed in X-rays but could not be confirmed in optical wavelengths. An outstanding example is the SNR B0532–67.5 in the Large Magellanic Cloud (LMC), the subject of this paper. We have chosen to study the LMC SNRs because their resolved underlying stellar population can be used to infer properties of supernova (SN) progenitors, especially for the core-collapse SNe.

SNR B0532–67.5 was first reported by Mathewson et al. (1985), who noted the absence of an associated optical shell structure, despite the presence of nonthermal radio emission and X-ray source. The diffuse X-ray emission from B0532–67.5 has been confirmed by ROSAT, Suzaku, and XMM-Newton observations and their spectral analyses show an interstellar abundance and an X-ray luminosity of a few $\times 10^{35}$ erg s^{-1} (Maggi et al. 2016; Takeuchi et al. 2016; Ramírez-Ballinas et al. 2019). Far

Ultraviolet Spectroscopic Explorer (FUSE) observations of B0532–67.5 did not detect the O VI $\lambda\lambda$ 1032, 1037 line emission (Blair et al. 2006). Spitzer Space Telescope observations did not detect any near- or mid-IR dust emission from this SNR (Seok et al. 2013), and the Herschel Space Observatory did not detect mid- to far-IR dust emission, either (Lakićević et al. 2015). It has been noted that SNR B0532–67.5 is likely associated with the OB association LH75, also known as NGC 2011 (Lucke & Hodge 1970; Chu 1997).

To understand the origin and evolution of SNR B0532–67.5, we have examined the stellar content of LH75 and explored its interstellar environment. This paper reports our investigation. Section 2 describes the multiwavelength observations used in this study, Section 3 examines the stars in LH75 to assess the SN progenitor’s mass, Section 4 analyzes the interstellar environment and its effects on the SNR’s physical properties, and Section 5 summarizes this work and its conclusions.

2. OBSERVATIONS

2.1. Available Photometric Catalogs of Stars

The *UBVI* photometric data of LH75 are from the Magellanic Cloud Photometric Survey (MCPS), which was made with the Great Circle camera on the Swope 1 m Telescope at Las Campanas (Zaritsky et al. 2004). These photometric data are used to construct color-magnitude diagrams (CMDs) in order to compare locations of stars with stellar evolutionary tracks to assess the massive star content of LH75.

To complement the MCPS photometry, We have also used the near-infrared *JHK_s* photometric data from the

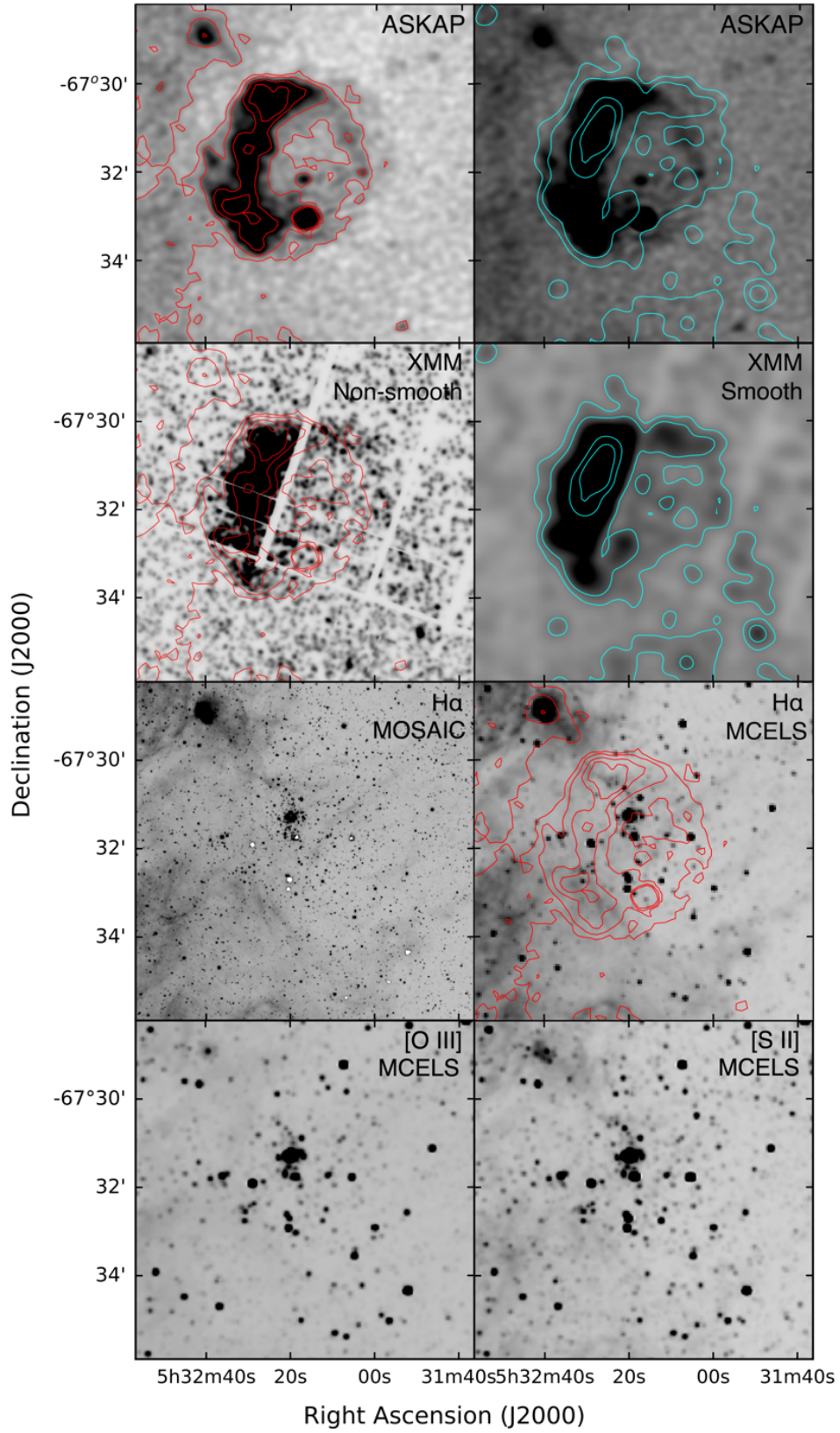


FIG. 1.— Multiwavelength images of SNR B0532–67.5. The origin of each image is marked in the upper right corner. The top row presents ASKAP 888 MHz continuum images, and the second row XMM-Newton X-ray images in the full energy band (0.1–15 keV). The bottom four images are CTIO 4m MOSAIC H α , MCELS H α , [O III], and [N II] images. To facilitate inter-comparisons, the contours of the ASKAP 888 MHz radio continuum image (left panel of the top row) are over-plotted on the XMM non-smoothed X-ray image and the MCELS H α image, and the contours of the XMM smoothed X-ray image are over-plotted on the ASKAP 888 MHz image (right panel of the top row).

InfraRed Survey Facility (IRSF) Survey (Kato et al. 2007) and the Two Micron All Sky Survey (2MASS; Skrutskie et al. 2006). The IRSF Survey of the Magellanic Clouds used the SIRIUS camera on the IRSF 1.4 m Telescope at the South African Astronomical Observatory, while the 2MASS used its 1.3 m telescope at Cerro Tololo Inter-American Observatory (CTIO) for the southern sky observations.

2.2. Surveys of the ISM

To investigate the ionized interstellar gas, we have used images from the Magellanic Cloud Emission Line Survey (MCELS; Smith & MCELS Team 1999). The MCELS survey used CCD cameras on the Curtis Schmidt 0.61 m Telescope at CTIO and imaged the Magellanic Clouds in the $H\alpha$, [O III], [S II] lines as well as a red continuum and a green continuum. For better resolution, we have also used an $H\alpha$ image taken with the MOSAIC camera on the Blanco 4 m Telescope at CTIO, as shown in Figure 1,

The H I interstellar gas in the LMC has been surveyed with the Australia Telescope Compact Array (ATCA) in conjunction with the Parkes Telescope observations (Kim et al. 2003). We have used this H I data cube to illustrate the cavities in the neighborhood of SNR B0532–67.5 and compare the H I velocities with those of ionized gas detected in the echelle observation that is described in the next subsection.

The hot, 10^6 K, ionized gas in the SNR B0532–67.5 was detected in an XMM-Newton X-ray observation (Obs. ID 0400320101; PI: R. Williams). This observation has been analyzed and reported by Maggi et al. (2016) and Ramírez-Ballinas et al. (2019). We will only present an X-ray image to illustrate the extent of hot ionized interstellar gas without repeating the X-ray spectral analysis of the hot gas properties. The exposure times for the EPIC-pn, MOS1, and MOS2 cameras are 42.6, 46.4, and 46.6 ks, respectively; however, after filtering out the high-background periods, the useful exposure times are 7.2, 10.6, and 12.1 ks, respectively (Ramírez-Ballinas et al. 2019).

The Australian Square Kilometre Array Pathfinder (ASKAP) has observed the general regions around SNR B0532–67.5 in the 888 MHz continuum with various configurations. We have found seven archival images that can be used to analyze the total intensity and polarization properties of SNR B0532–67.5. The relevant parameters of these seven ASKAP observations are summarized in Table 1. The top panels of Figure 1 show the 888 MHz continuum image from project AS033.

2.3. Echelle Observations of the Ionized Gas

To examine the kinematic properties of ionized gas around the SNR B0532–67.5, we obtained a long-slit high-dispersion spectroscopic observation with the echelle spectrograph on the Blanco 4 m Telescope at CTIO on 2001 December 25. The 79 l mm^{-1} echelle grating was used. For the long-slit single-order observing mode, a broad $H\alpha$ filter was used to isolate the order and the cross disperser grating was replaced by a flat mirror. The observation used a slitwidth of $250 \mu\text{m}$ (corresponding to $1''.64$) and an integration time of 1200 s. The data were recorded with the long-red camera and a SITe2K.6 2048×2048 CCD. The resulting echelle image

has pixel scales of $0.082 \text{ \AA pixel}^{-1}$ along the dispersion and $0''.26 \text{ pixel}^{-1}$ along the slit. Both the $H\alpha$ line and the [N II] $\lambda\lambda 6548, 6583$ doublet are detected.

3. ASSESSING SN PROGENITOR’S MASS

The SN progenitor of SNR B0532–67.5 may be a member of the OB association LH75; thus, we analyze the stellar content of LH75 and the surrounding field stars, in order to determine the origin of the progenitor and its possible stellar mass. The OB association LH75, or NGC 2011, has been studied as a cluster using either integrated cluster photometry or resolved stellar photometry. Its age determined from integrated photometry ranges from ~ 5 Myr (Hunter et al. 2003) to 14 Myr (Popescu et al. 2012), while its age determined from CMDs of resolved stars is higher, 20 Myr (Kumar et al. 2008) or 25 Myr (Glatt et al. 2010).

We have examined the MCPS *UBVI* photometric data, as well as the IRSF and 2MASS *JHK_s* photometric data, of resolved stars in LH75; however, we treat it as an OB association and place emphasis on only stars that are massive enough to end their lives in SNe. We made *V* versus $(B - V)$ CMD without extinction correction for all stars with $V < 17$ within $3'$ (or 45 pc) radius from the center of the SNR. Figure 2 shows the star field that we analyzed. It is clear that the field encompassed the entire OB association LH75, whose dimension is $3'$ (45 pc diameter) according to Lucke & Hodge (1970); furthermore, from comparisons with Figure 1 it can be seen that this star field generously encompasses the entire SNR B0532–67.5.

The *V* versus $(B - V)$ CMD of the above-mentioned star field is presented in Figure 3. The extinction toward LH75 is small, $E(B - V) = 0.08$ (Kumar et al. 2008), but not negligible; thus, we apply this extinction to the stellar evolutionary tracks for $Z = 0.008$ (closest to the LMC metallicity) from Lejeune & Schaerer (2001) and plot the reddened tracks in Figure 3. A closeup of the CMD for massive stars near the main sequence (MS) is presented in the right panel of this figure. Stars marked from A to R are candidates for the most massive stars in the field. They are marked in the $H\alpha$ image in Figure 2 as well as the CMDs in Figure 3. These 18 stars’ coordinates from MCPS, MCPS *UBVI*, and IRSF or 2MASS *JHK_s* magnitudes are compiled in Table 2. For each star, we compare its *UBV* and *JHK_s* colors and magnitudes with those of standard stars of luminosity classes V and I conveniently tabulated in Carroll & Ostlie (1996) and Sparke & Gallagher (2000) based on the original data from Schmidt-Kaler (1982). If a good match is found, the spectral type is adopted and given in the 11th column of Table 2. However, if the star has been spectroscopically classified and reported in the literature, its published spectral type is adopted and noted in the table.

The locations of stars in the *V* versus $(B - V)$ CMD are compared with the stellar evolutionary tracks to assess the stellar masses. These estimated stellar masses are given in the 12th column of Table 2. The uncertainty in the mass estimates may be 2–3 M_{\odot} for stellar masses below $10 M_{\odot}$, but the uncertainty is much larger for high-mass stars and may be 5 M_{\odot} or even higher. Detailed notes on our estimation of initial mass of each star are given in the Appendix.

TABLE 1
SUMMARY OF THE ASKAP OBSERVATIONAL PARAMETERS

Project ID	Sideband ID	Obs Date	Integration Time (s)	Beam Size & P.A.	Stokes
AS107 ^a	11125	2020 Jan 10	727	34'' × 32'', 37°	I,Q,U,V
	11546	2020 Jan 24	727	34'' × 32'', 0°	I,Q,U,V
	11570	2020 Jan 25	727	34'' × 32'', 0°	I,Q,U,V
	15665	2020 Aug 29	717	34'' × 32'', 26°	I,Q,U,V
	25517	2021 Apr 01	727	34'' × 32'', -10°	I,Q,U,V
AS113 ^b	10905	2019 Dec 19	727	34'' × 32'', 22°	I,Q,U,V
AS033 ^c	8532	2019 Apr 20	45,476	14'' × 12'', -84°	I

^a From [Murphy et al. \(2020\)](#).

^b From [Hotan et al. \(2020\)](#).

^c From [Harvey-Smith et al. \(2016\)](#).

The most massive star in the star field is C (30–35 M_{\odot}), outside LH75. The next most massive stars, in the 18–20 M_{\odot} range, are A, F, H, L, and N. It is very interesting that these most massive stars are all located to the southwest of LH75, as seen in Figure 2. None of them are near the core of LH75, where stellar masses are almost all $\leq 15M_{\odot}$. There is an apparent mass segregation.

Mass segregation in a young star cluster has been predicted from numerical simulations (e.g., [Dib et al. 2010](#); [Haghi et al. 2015](#)); however, massive stars are expected to concentrate at the center, contrary to what we see in LH75, and observational evidence of mass segregation in clusters has often been reported to be absent (e.g., [Elson et al. 1987](#); [Ascenso et al. 2009](#)). The reality may be that some clusters show mass segregation and some do not ([Schilbach et al. 2006](#)). In a detailed analysis of the LMC cluster NGC 1818, [de Grijs et al. \(2002\)](#) show that an excess number of bright stars are present around the cluster and suggest massive stars were ejected from the cluster core. The mass segregation in NGC 1818 is similar to what we observe in LH75.

To understand the mass segregation and to assess the relationship among LH75, massive stars to its southwest, and the SN progenitor, we plot isochrones on the CMD in Figure 4 to estimate the ages of the stars. It can be seen that the massive stars (A, C, F, H, L, and N) to the southwest of LH75 are all less than about 10 Myr old, while stars in the core of LH75 (I, J, and K) are 20–25 Myr old. The MS turnoff of LH75 is also consistent with an age of 20–25 Myr. The different ages indicate that the massive stars cannot be ejected from LH75. In fact, such juxtaposition of two stellar populations with different ages is frequently seen in star-forming regions where massive young stellar objects are detected along the periphery of superbubbles blown by OB associations (e.g., [Chen et al. 2009](#); [Carlson et al. 2012](#)). The formation of superbubbles requires energy feedback from both fast winds and SN explosions; therefore, there should be several Myr age difference between the central OB association and the stars subsequently formed through the superbubble compression of ambient ISM.

The key question to ask is thus whether the SN progenitor of B0532–67.5 was a member of LH75 or one of the massive stars formed through the energy feedback of LH75. To estimate the site of SN explosion, we first considered the outermost boundary of the X-ray and radio emission. The shock advances faster in low-density directions and the large contrast between the bright east rim

and the very faint northwest rim indicates the explosion site must be closer to the bright east rim. We then considered the overall bright radio rim of SNR B0532–67.5. Despite the surface brightness variations, the shape of the bright radio rim is elliptical and regular, and its center can be easily assessed. We adopt the center of the ellipse as the site of SN explosion and mark it by a cross in Figure 2. Note that the real SN explosion site may be closer to the bright east rim than our adopted center. It can be seen that the center of the SNR is closer to the core of LH75 than the group of massive stars that are less than 10 Myr old. Even if the SN site should be closer to the brightest part of the rim, which is east of LH75 and northeast of our adopted center, the SN site is still closer to LH75 than the group of massive stars. Therefore, we suggest that B0532–67.5’s SN progenitor was more likely a member of the OB association LH75 and its mass was close to $\sim 15 M_{\odot}$. In the less likely case that the SN progenitor belonged to the group of massive stars to the southwest of LH75, its mass would have been $\gtrsim 20M_{\odot}$.

4. MULTIPHASE INTERSTELLAR ENVIRONMENT

4.1. Multiwavelength Morphology of the SNR

SNR B0532–67.5 was first identified by its shell-like nonthermal radio emission ([Mathewson et al. 1985](#)). The ASKAP 888 MHz continuum image in Figure 1 indeed exhibits a complete shell structure with the eastern side significantly brighter than the western side. Superposed on the south rim of the radio shell is a bright compact source that corresponds to the cataloged radio source SUMSS J053215–673308 ([Mauch et al. 2003](#)). This compact radio source has no X-ray counterpart; furthermore, three other comparable compact radio sources without obvious counterparts are observed within 10' from the SNR. It is likely that the compact radio source on the south rim of SNR B0532–67.5 and the other three compact sources are all associated with background quasars or radio galaxies. This compact radio source will not be discussed further in this paper.

XMM-Newton X-ray image of SNR B0532–67.5 exhibits a shell qualitatively similar to the radio shell but different in surface brightness distribution. For easier comparisons between radio and X-ray emissions, we have plotted X-ray contours over the radio image in Figure 1. The X-ray surface brightness of SNR B0532–67.5 is the highest in the northeast quadrant and not detected in the southwest quadrant. The outer boundary of the X-ray

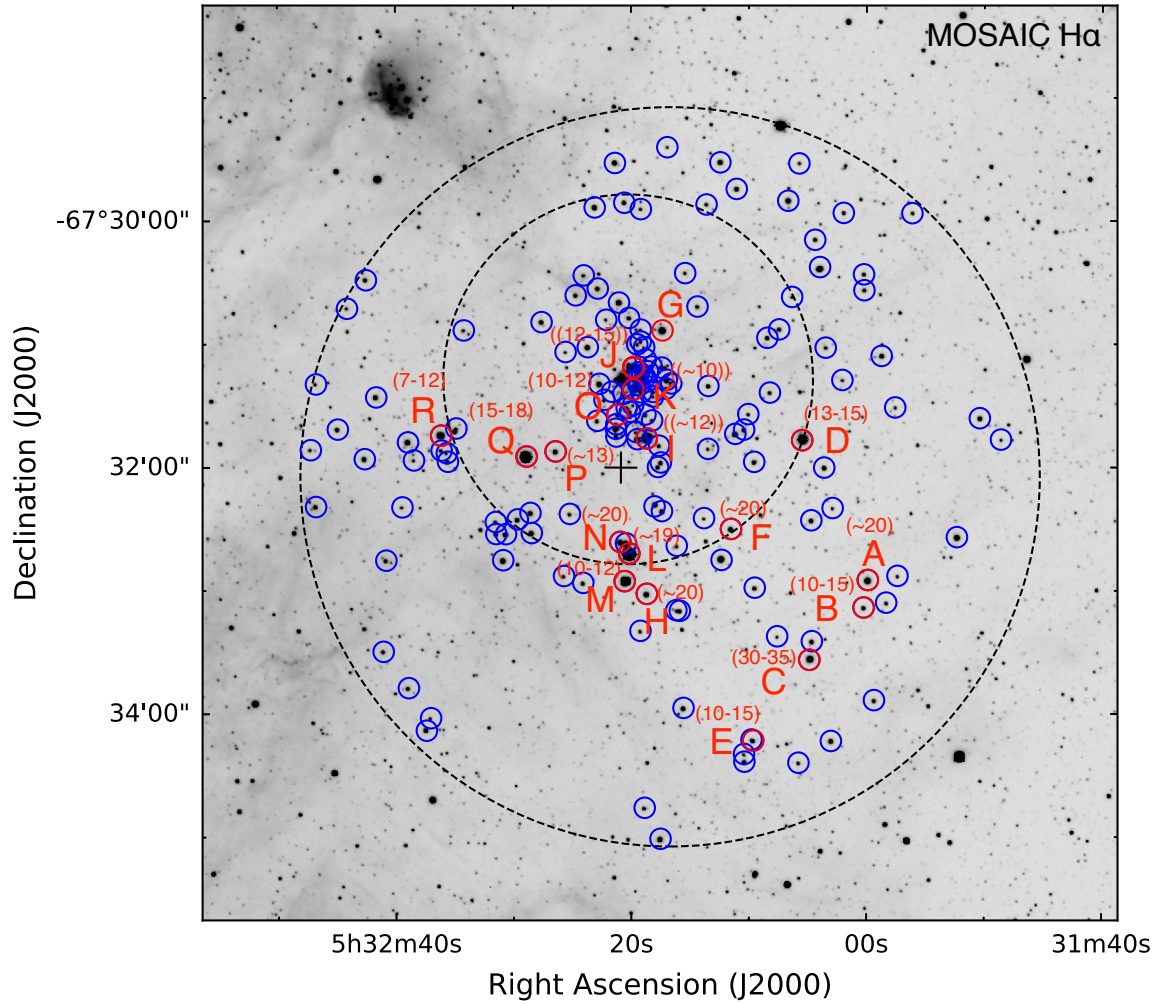


FIG. 2.— $H\alpha$ image of SNR B0532–67.5 showing the star field. A small dashed circle with a radius of $1'5$ (or 22.5 pc) is drawn around the OB association LH75. A large dashed circle with a radius of $3'$ (or 45 pc) is drawn around the SNR and encompasses the star field analyzed. The center of the SNR is marked by “+”. Within this field stars with $V < 17$ mag are marked with blue circles and used to construct the CMDs. Candidates for the most massive stars are marked with red circles and labeled from A to R. The numbers in parentheses above the labels are their estimated masses in units of M_{\odot} . Stars that are multiple or confused have larger uncertainties in their masses, and they are marked with double parentheses.

emission is similar to that of the radio emission, except where the X-ray emission is not detected. In the north-west quadrant, the X-ray image shows a simple rim, while the radio image shows a bright ridge that contributes to the ring morphology, and exterior to the ridge is a fainter extension that is coincident with the X-ray rim.

SNR B0532–67.5 is well known for its lack of an optical shell structure. As shown in Figure 1, no shell structure is seen in either H α or forbidden line images. However, when we plot the radio contours over the H α image, we can see enhanced H α emission along the brightest portion of the radio shell rim, especially in the north and southeast directions. These H α emission regions may be associated with the SNR, but may not be compressed by strong shocks, since no narrow filaments are seen.

The H I map provides the best depiction of the large-scale interstellar environment of SNR B0532–67.5. Figure 5a shows an H I column density map extracted from the ATCA+Parkes data cube (Kim et al. 2003) overplotted with the ASKAP 888 MHz continuum contours. It is quite evident that the SNR is in a cavity that is connected with the much larger cavity in the supergiant shell LMC-4 to the north (Meaburn 1980; Book et al. 2008). The position-velocity plot in Figure 5b shows even more unambiguously that the cavity is a true void. A close-up comparison between the ASKAP 888 MHz continuum image and the ATCA+Parkes H I column density map is presented in Figure 6. It is clear that the brightest radio and X-ray emission originates from areas where the SNR meets the H I cavity wall.

4.2. Hot Gas in the SNR Interior

The XMM-Newton X-ray observation of SNR B0532–67.5 has been analyzed by Maggi et al. (2016). They used non-equilibrium ionization (NEI) models to fit the integrated X-ray spectrum of the SNR, and the best-fit model has a plasma temperature of $kT = 0.53_{-0.11}^{+0.29}$ keV and an emission measure of $2.3_{-1.34}^{+3.53} \times 10^{58} \text{ cm}^{-3}$. The emission measure is $\int N_e^2 dV$, where N_e is the electron density and V is the emitting volume. Assuming a uniform hot gas with a filling factor of f , the emission measure can be expressed as $N_e^2 V f$. Adopting their plasma parameters and X-ray size of the SNR (285'' diameter), and a helium to hydrogen number density ratio $N_{\text{He}}/N_{\text{H}} = 0.1$, we derive an rms electron density of $0.064_{-0.023}^{+0.037} f^{-1/2} \text{ cm}^{-3}$. The total hot gas mass is $1.17 N_e m_{\text{H}} V f$, where m_{H} is the mass of a hydrogen atom, and is $350_{-125}^{+200} f^{1/2} M_{\odot}$ for SNR B0532–67.5. This large mass indicates that the hot gas is dominated by the swept-up interstellar medium (ISM). The total thermal energy in the hot gas is $(3/2)NkTVf$, where $N \sim N_e + N_{\text{H}} + N_{\text{He}} \sim 1.92N_e$, and is $4.5_{-1.9}^{+3.2} \times 10^{50} f^{1/2}$ ergs for SNR B0532–67.5.

SNR B0532–67.5 is in a low-density environment. It would be of interest to compare its hot gas properties to those of SNRs in a normal diffuse medium, such as the N206 SNR, which has also been analyzed by Maggi et al. (2016). The plasma temperature of N206, $kT = 0.52_{-0.04}^{+0.05}$ keV, is very similar to that of B0532–67.5; with a size of 180'', N206 is smaller than B0532–67.5, and the emission measure of N206, $1.63_{-0.16}^{+0.21} \times 10^{58} \text{ cm}^{-3}$, is also lower than B0532–67.5. Using these plasma parameters

of N206, we find that N206 SNR's hot gas density is ~ 1.7 times as high as that of SNR B0532–67.5, but the total thermal energy is only 0.43 times that of B0532–67.5. Apparently the presence or absence of an H α shell of a SNR does not cause more than a factor of ~ 2 effects on the hot gas properties.

4.3. Kinematics of the Superposed Interstellar Gas

We use the long-slit echelle observation to probe the warm (10^4 K) ionized gas superposed on SNR B0532–67.5. Figure 7 shows the slit position marked on the MOSAIC H α image and echelle images of the H α and [N II] $\lambda 6583$ lines. Although the H α image does not show much appreciable nebular emission, the echelle image detects the H α emission nicely. The H α line shows a narrow component at a constant velocity of $\sim 275 \text{ km s}^{-1}$ and a broad irregular component. The narrow component is actually the telluric OH 6-1 P2(3.5) line at 6568.779 Å (Osterbrock et al. 1996). Only the broad component originates from ionized gas in the LMC and is relevant here. This broad component has a great deal of velocity and width variations along the slit. Overall the H α line has a centroid near 300 km s^{-1} , similar to the bulk H I gas associated with the N57 H II complex to the south of the SNR. The broadest wings of the H α line has a full-width-at-zero-intensity approaching 80 km s^{-1} . Such line profiles are quite common for diffuse ionized ISM in the disk of a galaxy, and the line broadening is caused by a combination of large-scale motion and turbulence. An example of such broad line profile can be seen in the slit position EII-5 outside the supergiant shell LMC-2 reported by Points et al. (1999).

We have extracted an H I position-velocity diagram along the echelle slit position and present it along the H α echellogram in Figure 8. The velocity structures in the H I gas and H II gas are quite different. The H I 21 cm line shows line splittings that are most likely associated with large-scale structures, while the H α line shows broad asymmetric velocity profiles without line splitting. Considering that the isothermal sound velocity of 10^4 K ionized gas is $\sim 10 \text{ km s}^{-1}$ and that the width of the H α line is quite supersonic, the absence of line splitting indicates that the motion is dominated by turbulence rather than organized expansion. Evidently the ionized H II gas and the neutral H I gas do not have the same kinematic origin; furthermore, the SNR most likely has impacted the H II, rather than the H I, kinematics. It is not clear whether and how the velocity structure of the H α line is affected by the SNR B0532–67.5.

4.4. Magnetic Field in the SNR

The ASKAP 888 MHz images in Stokes I, Q, U, and V can be used to probe the magnetic field in B0532–67.5. We have smoothed these images to a beam size of $35'' \times 35''$, averaged images in respective Stokes parameters, and made an image cube of these four averaged maps. Figure 9a shows an image of the degree of polarization ($\sqrt{Q^2 + U^2}/I$) superposed by contours of polarized emission ($\sqrt{Q^2 + U^2}$) and polarization vectors. Figure 9b shows the Stokes I image (total intensity) superposed by contours of polarized emission. As the magnetic field direction is perpendicular to the polarization vector, we rotate the polarization vector by 90° and plot

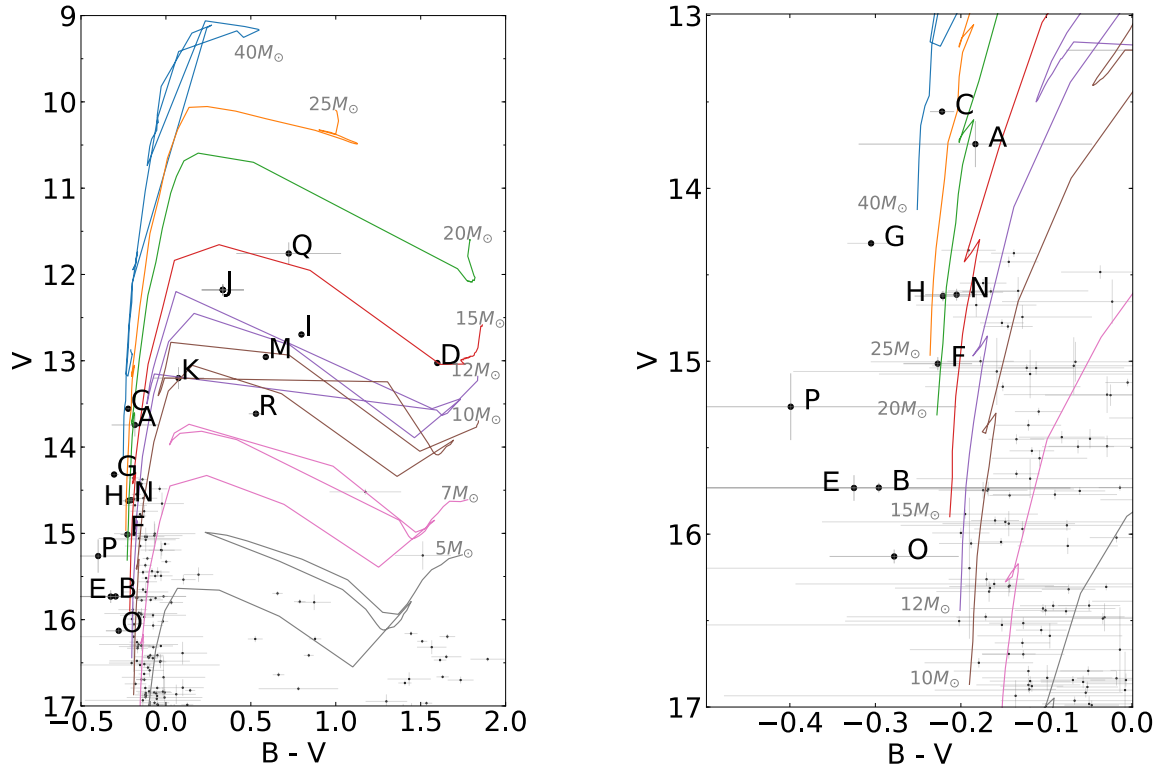


FIG. 3.— Left: V versus $B - V$ CMD of stars with $V < 17$ mag projected in and around SNR B0532–67.5. The MCPS photometric data (Zaritsky et al. 2004) are used. The evolutionary tracks of stars for $Z = 0.008$ from Lejeune & Schaerer (2001) are reddened by $E(B - V) = 0.08$ and plotted. The most massive star candidates are marked from A to R both in the CMDs and in the image in Figure 2. Right: close-up V versus $B - V$ CMD near the main-sequence of evolutionary tracks.

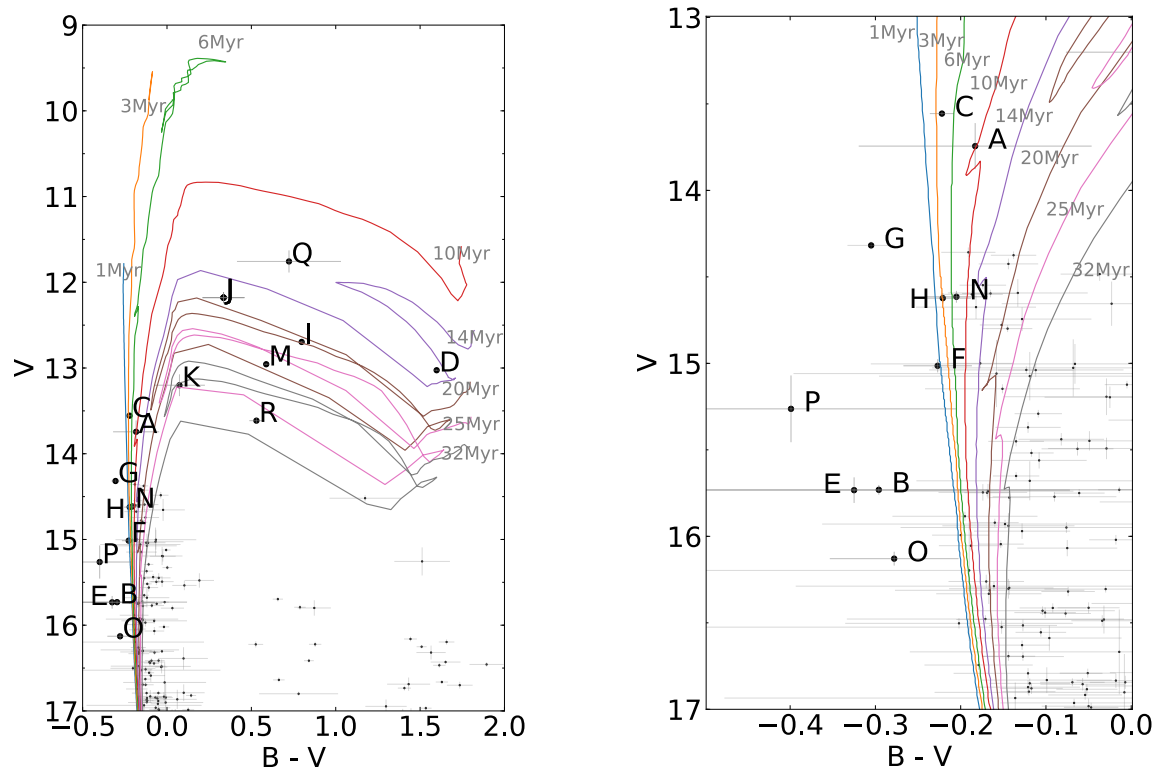


FIG. 4.— Same as Figure 3, except that isochrones for $Z = 0.008$ from Lejeune & Schaerer (2001) are reddened by $E(B - V) = 0.08$ and plotted.

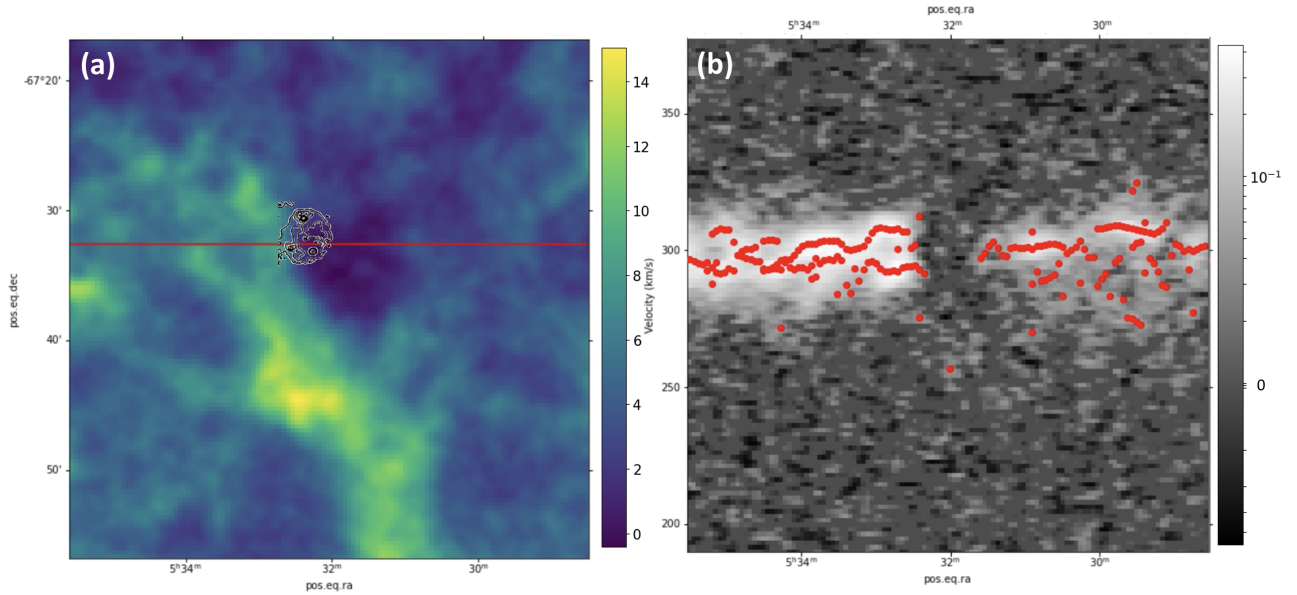


FIG. 5.— (a) ATCA/Parkes HI moment 0 map (color) integrated over a velocity range of $V_{\text{LSR}} = 243 - 348 \text{ km s}^{-1}$, superposed with contours extracted from the ASKAP 888 MHz radio continuum image (AS033) at levels of 0.40, 1.55, 2.70, 3.85, and 5.00 mJy beam^{-1} . The unit of the color bar is $\text{Jy beam}^{-1} \text{ km s}^{-1}$. (b) H I position-velocity diagram along the red line marked in (a). A log scale is used in the image, and the unit of the color bar is Jy beam^{-1} . The red dots denote the peak positions of each Gaussian component in the multi-component Gaussian fitting.

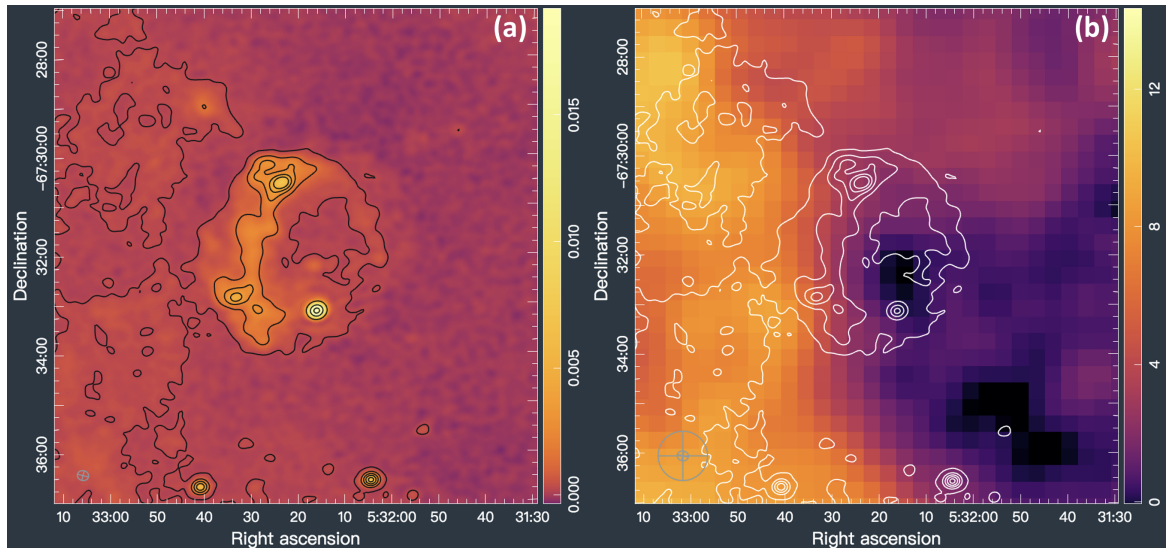


FIG. 6.— (a) ASKAP radio 888 MHz continuum image of B0532–67.5 with contours at levels of 0.40, 1.55, 2.70, 3.85, and 5.00 mJy beam^{-1} . Three additional contour levels of 6.00, 17.0, and 28.0 mJy beam^{-1} are plotted for the bright compact source. The unit of the color bar is mJy beam^{-1} . (b) A close-up of Figure 5(a) centered at SNR B0532–67.5. A log scale is used in this image, and the unit of the color bar is $\text{Jy beam}^{-1} \text{ km s}^{-1}$. The radio contours are the same as those in panel (a).

them over the image in Figure 9b.

It is interesting to note that the polarized emission is stronger toward the inner wall of the radio shell, where the H I column density is lower (see Fig. 6). The large size of SNR B0532–67.5 implies that it is old. In evolved old SNRs, the SNR shell consists of the ambient ISM compressed by radiative shocks (Dubner & Giacani 2015), and thus the magnetic field is expected to be tangential to the SNR shell (e.g. Milne 1968, 1987; Landecker et al. 1999; Wood et al. 2008; Dubner & Gi-

acani 2015). In SNR B0532–67.5 polarized radio emission is detected only in the bright eastern half of the shell. The magnetic field direction derived from the polarization vectors is parallel to the shell rim in the northern and southern parts of the polarized component, but appears to be perpendicular to the shell in the middle. This mixed magnetic field directions indicate that the polarization vectors could have been affected by foreground Faraday rotation. Radio observations of SNR B0532–67.5 in more wavelengths are needed to investi-

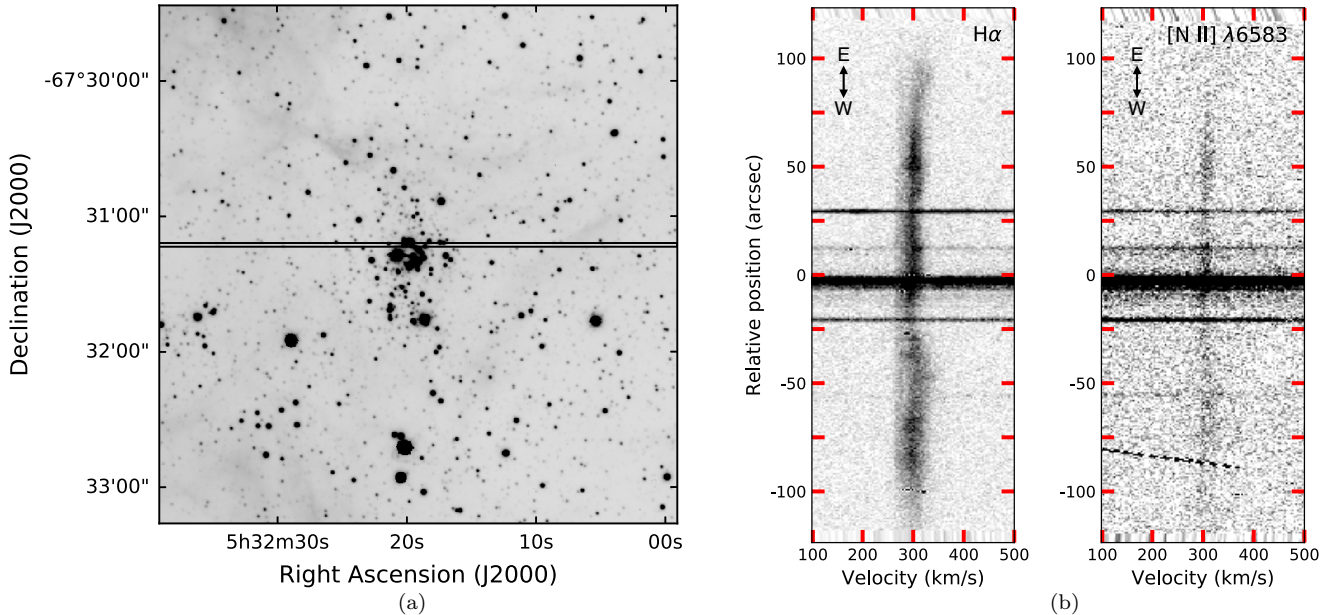


FIG. 7.— (a) The 4 m MOSAIC H α image of B0532–67.5 marked with the CTIO echelle slit position. (b) H α and [N II] echellograms of the slit position marked in (a). The slit orientation is marked in the upper left corner. Note that the lack of signal at the top and bottom ends of the slit is caused by vignetting in the optics of the echelle spectrograph.

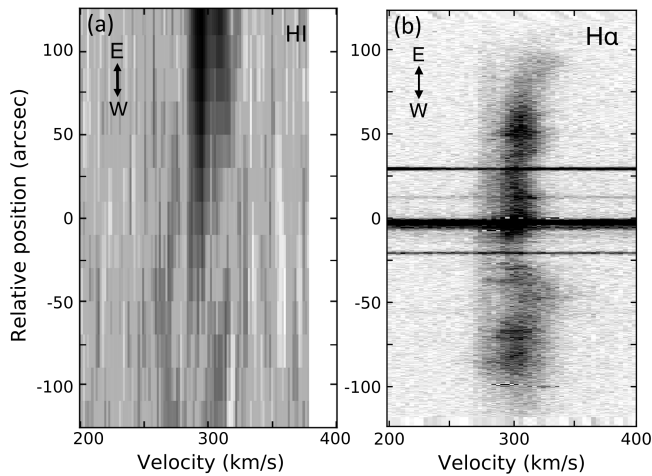


FIG. 8.— (a) H I position-velocity diagram extracted along the echelle slit position shown in Figure 7a. (b) Long-slit echelle image of the H α line rescaled for direct comparison with the H I velocity-position diagram in panel (a). Note that the narrow component at a constant velocity of ~ 275 km s $^{-1}$ is the telluric OH 6-1 P2(3.5) line. Only the broad component is valid emission from ionized gas in the LMC.

gate the magnetic field and foreground Faraday rotation.

5. SUMMARY AND CONCLUSIONS

The LMC is an ideal galaxy where SNRs can be studied in great detail; furthermore, the resolved underlying stellar population can be used to infer properties of SN progenitors, especially for the core-collapse SNe. This paper reports a detailed study of the SNR B0532–67.5. Its SNR nature was diagnosed by its nonthermal radio emission and confirmed by its diffuse X-ray emission; however, it does not exhibit any optical shell structure in either H α or forbidden lines.

We have analyzed the V versus $B - V$ CMD of stars brighter than $V = 17$ mag in and around SNR B0532–67.5, compared their locations in the CMD with evolutionary tracks to assess their initial masses, compared them with isochrones to estimate their ages, and examined their spatial distribution relative to the core of LH75. We find a segregation in stellar masses – the most massive stars (20–30 M_{\odot}) are distributed to the southwest and outside of LH75, while the stars in the core of LH75 have masses up to $\sim 15 M_{\odot}$. Comparisons with isochrones indicate that LH75 is 20–25 Myr old, while the massive stars to its southwest are less than 10 Myr old. It is possible that the energy feedback of LH75 compressed the ambient ISM and formed the massive stars to its southwest. The center of SNR B0532–67.5 is closer to the core of LH75 than the younger massive stars; therefore, we suggest that the SN progenitor was a member of LH75 and its initial mass was $\sim 15 M_{\odot}$. The low ambient interstellar density is responsible for the SNR’s lacking a visible shell structure in H α and forbidden lines.

XMM-Newton X-ray observations SNR B0532–67.5 were analyzed by Maggi et al. (2016), and we use their best-fit model to the X-ray spectrum to estimate the hot gas mass and thermal energy in the SNR interior. Assuming a filling factor of 0.1, the hot gas mass is $111^{+63}_{-40} M_{\odot}$ and the total thermal energy in the SNR interior is $1.4^{+1.0}_{-0.6} \times 10^{50}$ ergs, about 1/7 of a canonical SN explosion energy of 10^{51} ergs. This amount of thermal energy is within a factor of 2–3 similar to those in SNRs with visible H α shells of comparable SNR sizes, such as N206 and DEM L316A and DEM L316B (Williams et al. 2005; Williams & Chu 2005).

The ATCA + Parkes H I data cube of the LMC (Kim et al. 2003) is used to view the large-scale interstellar environment. SNR B0532–67.5 is associated with LH75 in the south end of the supergiant shell LMC-4 (Meaburn

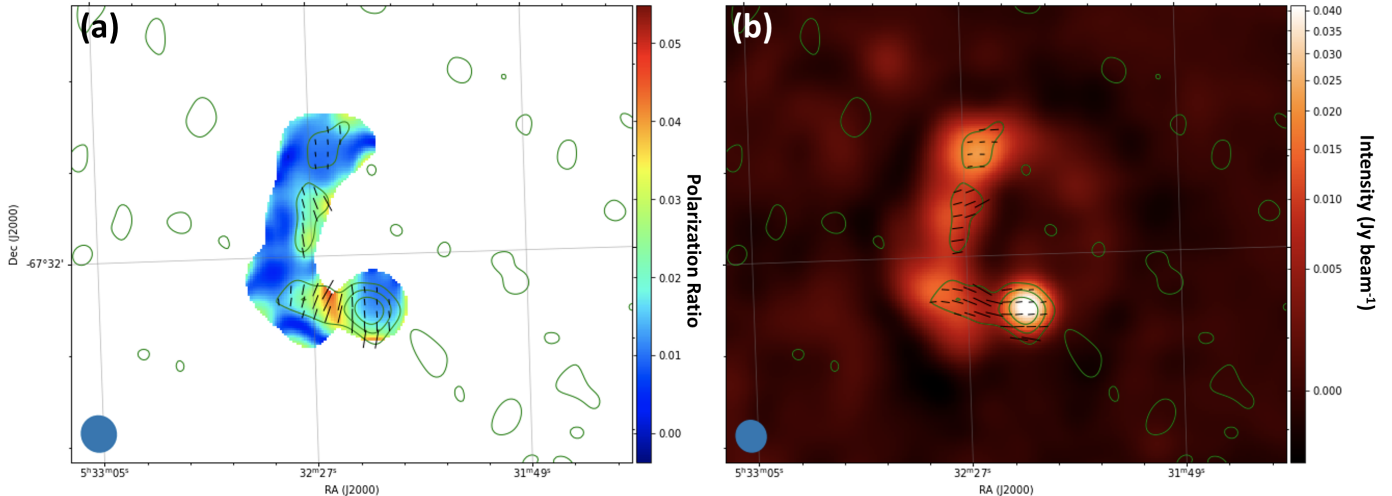


FIG. 9.— (a) ASKAP 888 MHz continuum degree of polarization (color), polarized emission (green contour), and polarized vector (black vector). The contour levels are 1.5, 2.5, 3.5σ where 1σ corresponds to $0.14 \text{ mJy beam}^{-1}$. The vector length denotes degree of polarization and the blue filled ellipse at the bottom left corner denotes the beam size, $35'' \times 35''$. (b) ASKAP 888 MHz continuum stoke I emission (color), polarized emission (green contour), and polarized vector rotated by 90° (black vector). The contour levels, vector length, and the beam size are the same as those in panel (a).

1980). The SNR is projected in an H I cavity with the brightest radio and X-ray rim abutting the H I wall. The H I cavity is apparently connected with the central cavity of the supergiant shell LMC-4 (Book et al. 2008). This large-scale structure of H I amply demonstrates an intricate relationship between the ISM structure and star formation history, and whether a core-collapse SN can produce an SNR with detectable optical signatures critically depends on the density of the ambient medium, which in turn depends on the star formation history and energy feedback.

This research is supported by the MOST grants 109-2112-M-001-040, 109-2811-M-001-545, 110-2112-M-001-020, and 110-2811-M-001-567 from the Ministry of Science and Technology of Taiwan.

The Australian SKA Pathfinder is part of the Australia Telescope National Facility which is managed by CSIRO. Operation of ASKAP is funded by the Australian Government with support from the National Collaborative Research Infrastructure Strategy. ASKAP uses the resources of the Pawsey Supercomputing Centre. Establishment of ASKAP, the Murchison Radio-astronomy Observatory and the Pawsey Supercomputing Centre are initiatives of the Australian Government, with support from the Government of Western Australia and the Science and Industry Endowment Fund. We acknowledge the Wajarri Yamatji people as the traditional owners of the Observatory site.

Software: SAOImage DS9 (Joye & Mandel 2003), astropy (Astropy Collaboration et al. 2018), matplotlib (Hunter 2007), numpy (van der Walt et al. 2011; Harris et al. 2020), scipy (Virtanen et al. 2020)

REFERENCES

- Astropy Collaboration, Price-Whelan, A. M., Sipőcz, B. M., et al. 2018, *AJ*, 156, 123. doi:10.3847/1538-3881/aabc4f
- Ascenso, J., Alves, J., & Lago, M. T. V. T. 2009, *A&A*, 495, 147. doi:10.1051/0004-6361/200809886
- Blair, W. P., Ghavamian, P., Sankrit, R., et al. 2006, *ApJS*, 165, 480. doi:10.1086/505346
- Book, L. G., Chu, Y.-H., & Gruendl, R. A. 2008, *ApJS*, 175, 165. doi:10.1086/523897
- Brunet, J. P., Imbert, M., Martin, N., et al. 1975, *A&AS*, 21, 109
- Carlson, L. R., Sewilo, M., Meixner, M., et al. 2012, *A&A*, 542, A66. doi:10.1051/0004-6361/201118627
- Carroll, B. W. & Ostlie, D. A. 1996, *An Introduction to Modern Astrophysics*, by B.W. Carroll and D.A. Ostlie. Benjamin Cummings, 1996. ISBN 0-201-54730-9.
- Chen, C.-H. R., Chu, Y.-H., Gruendl, R. A., et al. 2009, *ApJ*, 695, 511. doi:10.1088/0004-637X/695/1/511
- Chu, Y.-H. 1997, *AJ*, 113, 1815. doi:10.1086/118393
- Conti, P. S., Garmany, C. D., & Massey, P. 1986, *AJ*, 92, 48. doi:10.1086/114133
- Crawford, E. J., Filipović, M. D., Haberl, F., et al. 2010, *A&A*, 518, A35. doi:10.1051/0004-6361/201014767
- de Grijs, R., Johnson, R. A., Gilmore, G. F., et al. 2002, *MNRAS*, 331, 228. doi:10.1046/j.1365-8711.2002.05217.x
- Dib, S., Shadmehri, M., Padoan, P., et al. 2010, *MNRAS*, 405, 401. doi:10.1111/j.1365-2966.2010.16451.x
- Dubner, G. & Giacani, E. 2015, *A&A Rev.*, 23, 3. doi:10.1007/s00159-015-0083-5
- Elson, R. A. W., Fall, S. M., & Freeman, K. C. 1987, *ApJ*, 323, 54. doi:10.1086/165807
- Glatt, K., Grebel, E. K., & Koch, A. 2010, *A&A*, 517, A50. doi:10.1051/0004-6361/201014187
- Haghi, H., Zonoozi, A. H., Kroupa, P., et al. 2015, *MNRAS*, 454, 3872. doi:10.1093/mnras/stv2207
- Harris, C. R., Millman, K. J., van der Walt, S. J., et al. 2020, *Nature*, 585, 357. doi:10.1038/s41586-020-2649-2
- Harvey-Smith, Lisa; Chapman, Jessica; Lenc, Emil; McConnell, David; Ed-wards, Philip; Phillips, Chris; Sault, Bob; Reynolds, John; Heywood, Ian; Wark, Robin; Serra, Paolo; Chippendale, Aaron; Popping, Attila; Allison, James Richard; Indermuehle, Balthasar; Bell, Martin; Bannister, Keith; Bunton, John David; Kimball, Amy; Pro-copio, Pietro; Marquarding, Malte (2016): ASKAP Data Products for Project AS033(ASKAP Science Commissioning): images and visibilities. v1. CSIRO. Data Collection.http://hdl.handle.net/102.100.100/40062?index=1

- Hotan, Aidan; Whiting, Matthew; Huynh, Minh; Moss, Vanessa (2020): ASKAP Data Products for Project AS113 (Other ASKAP pilot science including tests, TOOs or guest observations): catalogues.v1.CSIRO. Data Collection. <http://hdl.handle.net/102.100.100/348894?index=1>
- Hunter, D. A., Elmegreen, B. G., Dupuy, T. J., et al. 2003, *AJ*, 126, 1836. doi:10.1086/378056
- Hunter, J. D. 2007, *Computing in Science and Engineering*, 9, 90. doi:10.1109/MCSE.2007.55
- Joye, W. A. & Mandel, E. 2003, *Astronomical Data Analysis Software and Systems XII*, 295, 489
- Kato, D., Nagashima, C., Nagayama, T., et al. 2007, *PASJ*, 59, 615. doi:10.1093/pasj/59.3.615
- Kim, S., Staveley-Smith, L., Dopita, M. A., et al. 2003, *ApJS*, 148, 473. doi:10.1086/376980
- Kumar, B., Sagar, R., & Melnick, J. 2008, *MNRAS*, 386, 1380. doi:10.1111/j.1365-2966.2008.12926.x
- Lakićević, M., van Loon, J. T., Meixner, M., et al. 2015, *ApJ*, 799, 50. doi:10.1088/0004-637X/799/1/50
- Landecker, T. L., Routledge, D., Reynolds, S. P., et al. 1999, *ApJ*, 527, 866. doi:10.1086/308100
- Lejeune, T. & Schaerer, D. 2001, *A&A*, 366, 538. doi:10.1051/0004-6361:20000214
- Lucke, P. B. & Hodge, P. W. 1970, *AJ*, 75, 171. doi:10.1086/110959
- Mathewson, D. S., Ford, V. L., Tuohy, I. R., et al. 1985, *ApJS*, 58, 197. doi:10.1086/191037
- Maggi, P., Haberl, F., Kavanagh, P. J., et al. 2016, *A&A*, 585, A162. doi:10.1051/0004-6361/201526932
- Massey, P. 2002, *ApJS*, 141, 81. doi:10.1086/338286
- Mauch, T., Murphy, T., Buttery, H. J., et al. 2003, *MNRAS*, 342, 1117. doi:10.1046/j.1365-8711.2003.06605.x
- Meaburn, J. 1980, *MNRAS*, 192, 365. doi:10.1093/mnras/192.3.365
- Milne, D. K. 1968, *Australian Journal of Physics*, 21, 201. doi:10.1071/PH680201
- Milne, D. K. 1987, *Australian Journal of Physics*, 40, 771. doi:10.1071/PH870771
- Muraveva, T., Clementini, G., Maceroni, C., et al. 2014, *MNRAS*, 443, 432. doi:10.1093/mnras/stu1151
- Murphy, Tara; Lenc, Emil; Bignall, Hayley; Bell, Martin; Reynolds, Cormac; Huynh, Minh; Bannister, Keith; Hotan, Aidan; Zic, Andrew; Dobie, Dougal; Kaplan, David; Qiu, Hao; Stewart, Adam; Brown, Ian (2020): ASKAP Data Products for Project AS107 (ASKAP Pilot Survey for VAST): catalogues.v1.CSIRO. Data Collection. <http://hdl.handle.net/102.100.100/340961?index=1>
- Osterbrock, D. E., Fulbright, J. P., Martel, A. R., et al. 1996, *PASP*, 108, 277. doi:10.1086/133722
- Ou, P.-S., Chu, Y.-H., Maggi, P., et al. 2018, *ApJ*, 863, 137. doi:10.3847/1538-4357/aad04b
- Points, S. D., Chu, Y. H., Kim, S., et al. 1999, *ApJ*, 518, 298. doi:10.1086/307249
- Popescu, B., Hanson, M. M., & Elmegreen, B. G. 2012, *ApJ*, 751, 122. doi:10.1088/0004-637X/751/2/122
- Ramirez-Ballinas, I., Reyes-Iturbide, J., Toalá, J. A., et al. 2019, *ApJ*, 885, 116. doi:10.3847/1538-4357/ab44cf
- Rousseau, J., Martin, N., Prévot, L., et al. 1978, *A&AS*, 31, 243
- Sanduleak, N. & Philip, A. G. D. 1977, *Publications of the Warner & Swasey Observatory*, 2, 105
- Schilbach, E., Kharchenko, N. V., Piskunov, A. E., et al. 2006, *A&A*, 456, 523. doi:10.1051/0004-6361:20054663
- Schmidt-Kaler, Th., "Physical Parameters of the Stars," *Landolt-Börnstein Numerical Data and Functional Relationships in Science and Technology*, New Series, Group VI, Volume 2b, Springer-Verlag, Berlin, 1982.
- Seok, J. Y., Koo, B.-C., & Onaka, T. 2013, *ApJ*, 779, 134. doi:10.1088/0004-637X/779/2/134
- Skrutskie, M. F., Cutri, R. M., Stiening, R., et al. 2006, *AJ*, 131, 1163. doi:10.1086/498708
- Smith, R. C. & MCELS Team 1999, *New Views of the Magellanic Clouds*, 190, 28
- Sparke, L. S. & Gallagher, J. S. 2000, *Galaxies in the Universe*, by Linda S. Sparke and John S. Gallagher, III, pp. 416. ISBN 0521592410. Cambridge, UK: Cambridge University Press, September 2000., 416
- Takeuchi, Y., Yamaguchi, H., & Tamagawa, T. 2016, *PASJ*, 68, S9. doi:10.1093/pasj/psv127
- van der Walt, S., Colbert, S. C., & Varoquaux, G. 2011, *Computing in Science and Engineering*, 13, 22. doi:10.1109/MCSE.2011.37
- Virtanen, P., Gommers, R., Oliphant, T. E., et al. 2020, *Nature Methods*, 17, 261. doi:10.1038/s41592-019-0686-2
- Westerlund, B. 1961, *Uppsala Astronomical Observatory Annals*, 5, 1
- Westerlund, B. E., Olander, N., & Hedin, B. 1981, *A&AS*, 43, 267
- Williams, R. M. & Chu, Y.-H. 2005, *ApJ*, 635, 1077. doi:10.1086/497681
- Williams, R. M., Chu, Y.-H., Dickel, J. R., et al. 2005, *ApJ*, 628, 704. doi:10.1086/431349
- Wood, C. A., Mufson, S. L., & Dickel, J. R. 2008, *AJ*, 135, 2358. doi:10.1088/0004-6256/135/6/2358
- Zaritsky, D., Harris, J., Thompson, I. B., et al. 2004, *AJ*, 128, 1606. doi:10.1086/423910

TABLE 2
BRIGHTEST MASSIVE STARS IN AND NEAR SNR B0532–67.5 FROM THE MCPS DATA

Star	R.A. (J2000)	Decl. (J2000)	<i>U</i>	<i>B</i>	<i>V</i>	<i>I</i>	<i>J</i>	<i>H</i>	<i>Ks</i>	Spectral Type	Mass (M_{\odot})
A	05:31:59.88	-67:32:54.92	12.54 ± 0.03	13.56 ± 0.03	13.74 ± 0.13	14.01 ± 0.04	14.30 ± 0.01	14.35 ± 0.02	14.41 ± 0.02	O9.5 III ^a	~20
B	05:32:00.24	-67:33:08.32	14.77 ± 0.06	15.44 ± 0.41	15.73 ± 0.03	15.96 ± 0.03	16.21 ± 0.02	16.23 ± 0.02	16.36 ± 0.08	B2 V ^b	10–15
C	05:32:04.85	-67:33:33.80	12.32 ± 0.01	13.33 ± 0.01	13.56 ± 0.01	13.71 ± 0.06	14.00 ± 0.01	14.06 ± 0.01	14.11 ± 0.02	B0 II ^a	30–35
D	05:32:05.47	-67:31:46.88	16.29 ± 0.06	14.62 ± 0.01	13.03 ± 0.01	-	10.19 ± 0.02 ^c	9.42 ± 0.03 ^c	9.19 ± 0.02 ^c	K4 I ^b	13–15
E	05:32:09.63	-67:34:13.08	14.47 ± 0.03	15.41 ± 0.24	15.73 ± 0.07	15.76 ± 0.06	16.19 ± 0.03	16.25 ± 0.03	16.39 ± 0.09	B0–1 V ^b	10–15
F	05:32:11.51	-67:32:30.08	13.82 ± 0.08	14.79 ± 0.01	15.01 ± 0.04	15.23 ± 0.03	15.45 ± 0.01	15.53 ± 0.02	15.55 ± 0.04	B0 V ^b	~20
G ^d	05:32:17.33	-67:30:53.42	13.11 ± 0.03	14.01 ± 0.02	14.32 ± 0.02	13.87 ± 0.04	13.92 ± 0.01	13.85 ± 0.01	13.70 ± 0.02	-	-
H	05:32:18.66	-67:33:01.70	13.53 ± 0.04	14.40 ± 0.01	14.62 ± 0.03	14.76 ± 0.03	14.87 ± 0.01	14.82 ± 0.01	14.79 ± 0.03	-	~20
I	05:32:18.67	-67:31:45.98	13.04 ± 0.01	13.49 ± 0.01	12.70 ± 0.01	-	9.71 ± 0.02 ^c	8.94 ± 0.03 ^c	8.64 ± 0.03 ^c	-	~12
J ^e	05:32:19.80	-67:31:11.46	11.82 ± 0.10	12.51 ± 0.11	12.18 ± 0.07	12.53 ± 0.15	15.23 ± 0.03	14.78 ± 0.11	-	-	12–15
							14.61 ± 0.07	14.18 ± 0.04	13.92 ± 0.07		
							14.72 ± 0.06	-	-		
							15.41 ± 0.06	15.45 ± 0.07	15.44 ± 0.13		
K	05:32:19.82	-67:31:22.12	12.37 ± 0.07	13.28 ± 0.08	13.20 ± 0.13	-	13.87 ± 0.02	-	-	-	~10
L	05:32:20.16	-67:32:42.04	-	15.52 ± 0.02	12.98 ± 0.12	9.7 ^f	9.22 ± 0.03 ^c	8.37 ± 0.03 ^c	8.01 ± 0.04 ^c	M2 I ^f	~19
M	05:32:20.55	-67:32:55.50	13.94 ± 0.01	13.54 ± 0.01	12.96 ± 0.01	-	11.77 ± 0.01	11.50 ± 0.01	11.45 ± 0.02	F8 I ^b	10–12
N	05:32:20.92	-67:32:36.38	13.51 ± 0.29	14.41 ± 0.01	14.62 ± 0.03	14.94 ± 0.23	-	15.26 ± 0.06	-	-	~20
O	05:32:21.16	-67:31:34.50	15.10 ± 0.08	15.85 ± 0.06	16.13 ± 0.04	15.96 ± 0.08	16.62 ± 0.03	16.66 ± 0.04	16.71 ± 0.11	B2 V ^b	10–12
P	05:32:26.41	-67:31:52.32	14.24 ± 0.04	14.86 ± 0.02	15.26 ± 0.19	15.44 ± 0.22	15.65 ± 0.01	15.70 ± 0.02	15.80 ± 0.05	B1 V ^b	~13
Q	05:32:28.87	-67:31:54.77	10.89 ± 0.14	12.48 ± 0.28	11.76 ± 0.13	-	11.84 ± 0.01	11.81 ± 0.01	11.73 ± 0.02	B8 I ^g	15–18
R	05:32:36.13	-67:31:44.58	14.04 ± 0.03	14.14 ± 0.02	13.61 ± 0.04	12.81 ± 0.13	12.63 ± 0.01	12.35 ± 0.01	12.33 ± 0.02	-	7–12

^a From Conti et al. (1986); Massey (2002).

^b This paper; photometrically estimated.

^c From 2MASS.

^d Colors are poorly fitted with stellar atmosphere model in the MCPS data.

^e Multiple stars. The mass estimated from the CMD and stellar evolutionary tracks has large uncertainties and represents an upper limit.

^f From Westerland et al. (1981).

^g From Rousseau et al. (1978).

Appendix: Notes on individual stars:

The mass estimates of stars are approximate. The uncertainty in the mass estimates may be 2–3 M_{\odot} for stellar masses below 10 M_{\odot} , but the uncertainty is much larger for high-mass stars and may be 5 M_{\odot} or even higher.

Star A. This star was cataloged as BI 192 and classified as OB0 by Brunet et al. (1975). The spectral type was later refined to O9.5 III (Conti et al. 1986; Massey 2002). This star has evolved off the main sequence (MS) and is located close to the evolutionary track of a 20 M_{\odot} star; therefore, we assign an initial mass of $\sim 20 M_{\odot}$.

Star B. This star has a large uncertainty in its B magnitude. Its colors in other passbands are similar to a B2 V star. Within its $B - V$ uncertainty, its location in the CMD could overlap the evolutionary tracks of 10–15 M_{\odot} star; thus we assign a stellar mass of 10–15 M_{\odot} .

Star C. This star was cataloged as BI 193 and classified as OB0 by Brunet et al. (1975). The spectral type was later refined to B0 II (Conti et al. 1986; Massey 2002). Its location in the CMD is between the evolutionary tracks of 25 and 40 M_{\odot} stars. We assign an initial mass of 30–35 M_{\odot} to this star.

Star D. This star was cataloged as W61 19-1 and classified as M star with large uncertainty by Westerlund (1961). We find that the colors and magnitudes of this star are similar to a K4 I star, which has an initial mass of $\sim 13 M_{\odot}$. This star’s location in the CMD is on the evolutionary track of a 15 M_{\odot} star. Thus, we assign an initial mass of 13–15 M_{\odot} to this star.

Star E. The colors and magnitudes of this star suggest a spectral type of B0–1 V. Its B magnitude has a larger error than the others, which may be the cause of its location bluer than the evolutionary tracks. Based on its likely spectral type of B0–1 V and its location in the CMD, we assign an initial stellar mass of 10–15 M_{\odot} .

Star F. The colors and magnitudes of this star are similar to a B0 V star. Its location in the CMD is close to the evolutionary track of a 20 M_{\odot} MS star. Thus, we assign an initial stellar mass of $\sim 20 M_{\odot}$.

Star G. This star was flagged in MCPS for colors poorly fitted by atmospheric models, as noted by Zaritsky et al. (2004). The combination of the MCPS $UBVI$ and IRSF JHK_s photometric data shows clearly that this object has a near-infrared excess, indicating the existence of a late-type companion. Spectroscopic observations are needed to reveal the nature of this system.

Star H. The colors of this star are similar to B1, but its M_V is 1.5 mag brighter than a B1 V star. The star is close to the evolutionary track of a 20 M_{\odot} star. We estimate a spectral type of B1 II and assign an initial stellar mass of 20 M_{\odot} .

Star I. This star is close to the core of LH75, and was cataloged as W61 19-14 without spectral classification. (Westerlund 1961). This star’s colors and magnitudes are complex and must contain multiple stars. Its location in the CMD suggests an evolved $\sim 12 M_{\odot}$ star.

Star J. This object is at the core of LH75. It has a single entry in the MCPS catalog, but the IRSF catalog lists four sources within 1" from the MCPS star position. Assuming that the optical emission is dominated by one star, its location in the CMD is between the evolutionary tracks of 12–15 M_{\odot} stars. We assign a mass of 12–15 M_{\odot} for the most massive star within this object.

Star K. This star is near the crowded core region of LH75, and its ground-based photometric measurements may have larger errors due to confusion. Its apparent UBV colors do not match any single MS or supergiant stars. If the photometric measurements indeed correspond to a single star, its location in the CMD indicates that it is an evolved star with an initial mass $\sim 10 M_{\odot}$.

Star L. This star was cataloged as W61 19-24 by Westerlund (1961), and as WOH S 383 by Westerlund et al. (1981), who also classified the star to be an M2 I red supergiant. With a $B - V = 2.54 \pm 0.14$, this star is off the chart in Figure 3. The mass of an M2 I star would be $\sim 19 M_{\odot}$.

Star M. The colors of this star are consistent with an F8 I, but about 1 mag fainter. Its location in the CMD is near the evolutionary tracks of 10 and 12 M_{\odot} stars. We assign a stellar mass of 10–12 M_{\odot} .

Star N. The colors of this star are similar to B1, but its M_V is 1.5 mag brighter than a B1 V star. The star is close to the evolutionary track of a 20 M_{\odot} star. We estimate a spectral type of B1 II and assign an initial stellar mass of 20 M_{\odot} .

Star O. The UBV colors suggest a B2 V spectral type, but about 1 mag brighter. The uncertainties in colors cannot exclude an earlier spectral type of B1 V. The star is probably 10–12 M_{\odot} .

Star P. The UBV photometry of this star has a large uncertainty in V . This large uncertainty is also reflected in its unreasonable location in the CMD. These uncertainties may be caused by its being an eclipsing binary (Muraveva et al. 2014). If we assume the star is on the MS, its V magnitude implies a spectral type close to B1 V, and the stellar mass would be $\sim 13 M_{\odot}$.

Star Q. This star, aka HD 269726 and Sk-67 178, is visually the brightest star within SNR B0532-67.5. Its colors and magnitudes do not match any standard stars. It was classified by Rousseau et al. (1978) to be of spectral type B8 I, which would suggest an initial stellar mass of $\sim 18 M_{\odot}$, although the star is closest to the evolutionary track of a $15 M_{\odot}$ star in Figure 3.

Star R. The colors and magnitudes of this star do not match any main sequence or supergiant stars. Its location in the CMD, compared with the stellar evolutionary tracks, suggests that it is an evolved star with an initial mass of 7-12 M_{\odot} .